Characterizing subsiding shells in shallow cumulus using Doppler lidar and large-eddy simulation

Lucas A. McMichael[1], Fan Yang[2], Tobias Marke[3,4], Ulrich Löhnert[5], David B. Mechem[1], Andrew M. Vogelmann[2], Kevin Sanchez[6,7], Minttu Tuononen[8,9], and Jan H. Schween[5]

1 Department of Geography and Atmospheric Science, University of Kansas, Lawrence, KS, USA

2 Environmental and Climate Sciences Department, Brookhaven National Laboratory, Upton, NY, USA

3 Cooperative Institute for Research in Environmental Sciences, University of Colorado, Boulder, CO, USA

4 NOAA/Earth System Research Laboratory, Chemical Sciences Laboratory, Boulder, CO, USA

5 Institute for Geophysics and Meteorology, University of Cologne, Cologne, Germany

6 Universities Space Research Association, Columbia, MD, USA

7 NASA Langley Research Center, Hampton, VA, USA

8 Finnish Meteorological Institute, Helsinki, Finland

9 Vaisala Oyj, Vantaa, Finland

Corresponding Author: Lucas A. McMichael (mcmichael@ku.edu)

Key Points

1. Doppler lidar indicates the presence of a vertically asymmetric subsiding shell in shallow cumulus that is on the order of 100 m wide.
2. Large-eddy simulations can reasonably reproduce observed shell structure and intensity.
3. Most of the asymmetry observed by lidar reflects fundamental cloud structures and is not simply a consequence of the sampling method.

Abstract

The existence of subsiding shells on the periphery of shallow cumulus clouds has major implications concerning the parameterization of shallow convection, with the mass exchange between the shell and cloudy air representing a significant deviation from the commonly used bulk-plume parameterization. We examine the structure and frequency of subsiding shells in shallow cumulus convection using Doppler lidars at the Atmospheric Radiation Measurement (ARM) Southern Great Plains (SGP) facility in the central USA, and at the Jülich ObservatorY for Cloud Evolution (JOYCE) in western Germany. Doppler lidar indicates that the vertical subsiding shell extent is asymmetric, while shell width is typically ~100 m. Large-eddy simulation can reasonably simulate the observed shell structure using a grid spacing of 10 m and suggests that much of the observed asymmetry is not a result of transient cloud evolution.

Plain Language Summary

Doppler lidars allow for the inference of vertical air motion. On the edges of the shallow "popcorn" cumulus clouds, regions of sinking air (subsiding shells) are observed. If we wish to understand how these clouds interact with their environment, we must understand the structure of the subsiding shells that envelop them. As a cloud passes over the lidar, the front edge of the cloud is sampled first and the back edge is sampled later. The back-edge subsiding shell descends farther below cloud base than the front-edge shell. High-resolution models can resolve the observed shell structure and suggest that the differences between the front and back-edge shells do not arise from the evolution of the cloud during the tens of seconds it takes to pass over the lidar.

1 Introduction

Despite efforts to create comprehensive Earth System Models (ESMs) that represent as many physical processes as possible, the wide spread of model responses to a doubling of CO_2 remains unchanged (Maslin and Austin, 2012; Stevens and Bony, 2013; Sherwood et al., 2014). The uncertainty regarding climate sensitivity has been largely attributed to the representation of clouds and the magnitude of the shortwave cloud-radiative feedback (Caldwell et al., 2016). A majority of the cloud-radiative feedback uncertainty stems from the sensitivity to changes in net low cloud amount and water content (Dufresne and Bony, 2008; Zelinka et al., 2016; Zelinka et al., 2020), which highlights the vital importance of understanding boundary-layer clouds.

Among boundary-layer clouds, the responses under warming scenarios are most questionable for shallow cumulus convection, with large-eddy simulations (LES) and convection-allowing global models producing opposing trends in low cloud amount (Wyant et al., 2009; Bretherton et al., 2013; Ceppi et al., 2017). Shallow cumulus are small residuals of the total water budget, but they exert an enormous influence on the global circulation through radiative feedbacks (Chen et al., 1999; Rossow and Schiffer, 1999) and the vertical redistribution of moisture and heat (Bony et al., 2015). Additionally, shallow cumulus can alter stratocumulus evolution through cumulus coupling (Bretherton and Wyant, 1997; Wood, 2012). Because shallow cumulus are much smaller (O(100 m) in horizontal extent) than the typical ESM grid spacing (O(50 km)), many of the processes that determine vertical mass flux in ESMs are tied to parameterized components of the model (turbulence and microphysics) that are under-constrained by physical laws and require assumptions and tunings.

ESMs traditionally represent shallow cumulus convection as an ensemble of steady-state entraining/detraining plumes (de Rooy et al., 2013). Each cloud element in the ensemble can be

dealt with individually (as Arakawa and Schubert (1974) do for deep convection) or, more commonly, the ensemble of clouds is averaged into a single updraft (bulk-plume method) with an entrainment rate that is either prescribed as a constant or based on some parametric relationship with the cloud/environmental properties (de Rooy et al., 2013). The foundational assumption of the bulk-plume method is that a clear distinction can be made between the buoyant plume and the environment, but this is challenged by the existence of substantial downward vertical velocities near the cloud edges (subsiding shells) (Jonker et al., 2008; Yano et al., 2015). Subsiding shells have been observed with aircraft (Jonas, 1990; Rodts et al., 2003; Katzwinkel et al., 2014), with the shell regions near cloud edge exhibiting dips in virtual potential temperature, increased turbulence, and significant downward mass transport. As Jonker et al. (2008) noted, observations are a considerable departure from the classical view whereby broad regions of subsidence warming act to reduce the horizontal buoyancy gradient between the plumes and the environment. Subsiding shells play a critical role in determining the mass exchange between the plume and the environment, which ultimately dictates the thermodynamic properties of the air entrained into the cloud.

The trend toward global cloud-resolving models (O(1 km)) presents several major challenges for the traditional mass-flux-based approaches (Satoh et al., 2019) where the standard assumption of quasi-steady-state equilibrium and typical statistical distributions of cloud size break down (Yano et al., 2015). Furthermore, with increasing resolution, clouds and subsiding shells cover a greater fraction of a model grid, and the classical assumption of a robust scale separation between the clouds and their environment is violated. Therefore, a physically reasonable representation of shallow convective mixing will need to account for the effects of subsiding shells.

In this study, we examine the structure and occurrence frequency of subsiding shells around cumuli using Doppler lidar data, which enable the detection of subsiding shells and analysis of the vertical velocity structure around the cloud edge and below cloud base (Ansmann et al., 2010; Lamer and Kollias, 2015; Lareau et al., 2018). Particularly, we focus on the asymmetries observed between the front and back edges of afternoon shallow cumulus clouds over two continental sites: the Atmospheric Radiation Measurement (ARM) Southern Great Plains (SGP) facility, and the Jülich ObservatorY for Cloud Evolution (JOYCE). The dependence of shell characteristics on updraft mass flux (positive/negative) is explored. The Doppler lidar results are compared with large-eddy simulation output to assess the ability of the model to represent the subsiding shell structures and to explain asymmetries found in observations.

2 Data and Methods

2.1 SGP and JOYCE Instrumentation

Doppler lidars are active sensors that emit infrared radiation (1.5 μm) and infer Doppler velocities from particle backscattering (aerosol or cloud) in the boundary layer. Vertical velocities are determined from zenith-pointing measurements and horizontal wind speed and direction can be deduced from full scans along a constant azimuth. At the SGP central facility in northern Oklahoma, USA (36.605˚N, 97.486˚W, 316 m MSL), a zenith-pointing HALO-Streamline lidar obtains vertical velocity with a range resolution of 30 m, a temporal resolution of approximately 1 s, and a precision of $\leq$0.1 ms^{-1} below 2 km (Newsom, 2012). The Doppler lidar operating at JOYCE in western Germany (50.908˚N, 6.414°E, 111 m MSL) has similar performance characteristics to the SGP lidar (Löhnert et al., 2015). At both sites, horizontal

winds near cloud base are obtained every 15 mins from a full azimuthal scan at a 75˚ elevation (Löhnert et al., 2015).

2.2 Cloud Detection and Selection

The selection of shallow cumulus days was performed manually, by visual inspection of boundary-layer attenuated backscatter time series, vertical-velocity time series, and merged data products such as Cloudnet (Illingworth et al., 2007) and ARSCL (Clothiaux et al., 2000; Kollias et al., 2005), which provide estimates of cloud-top height and cloud type. The preferred shallow cumulus environment for this study includes a summertime convective boundary layer with sparse cloudiness, weak synoptic forcing, no precipitation, and an absence of other cloud types. After applying these criteria, a total of 40 days at SGP and 86 days at JOYCE were chosen (DOI: 10.5281/zenodo.3774569). We performed automated cloud selection and edge detection on the selected shallow cumulus periods. Cloud bases and edges were detected as a backscatter threshold exceeding 10^{-4} $m^{-1}sr^{-1}$, which lowered the probability of false hits from non-cloudy targets compared to a more sensitive threshold (e.g., $6x10^{-5}$ $m^{-1}sr^{-1}$ used in Hogan et al., 2004). Cloud base was required to reside within an altitude range of 200-2000 m (AGL).

The properties of individual clouds were determined for each chosen day. The time series of backscatter profiles were converted into spatial cross-sections by first determining the existence of an isolated cloud chord, defined as a continuous string of cloudy profiles surrounded by clear air profiles. A cloud chord must consist of at least 10 continuous cloudy profiles and have 50 consecutive clear air profiles on each side of the cloud. The following procedure was used to provide an approximate transformation of chord length from the temporal to spatial domain. For each chord, the midpoint in time was determined and used to find the most recent

horizontal wind profile from the scanning mode of the lidar. The cloud base along the chord is then analyzed to determine the lowest cloud-base height. The horizontal velocity is extracted from one level below the minimum cloud-base height and applied as a mean wind throughout the cloud layer.

Altogether, 91 clouds were sampled at SGP and 208 at JOYCE. Clouds were classified as having a negative or positive mass-flux by averaging the vertical velocities one level below the minimum cloud-base height, with an average positive (negative) average value greater (less) than 0 ms^{-1} being classified as a positive (negative) mass-flux cloud. A subsiding shell is deemed present if at least two successive profiles outside the clouds' edges met a vertical velocity threshold of $\leq$ -0.1 ms^{-1}. The subsiding shell width is determined from the number of neighboring profiles that met the vertical velocity criteria. The requirement of two successive profiles imposes a lower bound on the possible shell width that is equal to twice the speed of the horizontal wind. A discussion of the observational limitations is included in the Supplemental Materials (Text S1).

2.3 LES Configuration and Virtual Lidar Setup

All simulations are performed with the System for Atmospheric Modeling (SAM), version 6.9.6 (Khairoutdinov and Randall, 2003). SAM prognoses two moist-adiabatically conserved thermodynamic variables (in the absence of precipitation): liquid water static energy (S_l) and total water mixing ratio (q_t). The vertical domain extends to 3.6 km, while the horizontal domain is 5.8 km^2, with doubly periodic horizontal boundary conditions. A uniform grid spacing of 10 m was used, with cloud-base vertical velocity PDFs (as calculated in Endo et al., 2019) exhibiting a minor sensitivity to grid spacing, with a modal shift of -0.1 ms^{-1} from 25 to 10 m

(see supplement Figure S1). All simulations employ the extensively-used LES case configuration developed from observations collected during the Barbados Oceanographic and Meteorological Experiment (BOMEX; Holland and Rassmusson, 1973). BOMEX represents a typical environment for marine shallow cumulus in the tropics and provides a statistically steady-state case to address how the observation method (lidar) may impact perceived cloud structures. After model spin-up, mean zonal shear through the cloud layer depth of ~1 km is ~2 ms^{-1}, with the shear vector being in the same direction as the mean wind (east-west winds). Details of the LES configuration can be found in the Supplemental Materials (Text S2).

The cloud structures and shell asymmetries are explored through the use of "virtual" lidars and "static" cross-sections to simulate two perspectives: one that recreates the observation of clouds advected overhead (as a lidar would observe), and one that instantaneously evaluates the cloud environment at the front and back edges (i.e., "static" clouds). Since the vertical velocity in the LES is not derived from the motion of aerosols, the virtual lidar output simply uses a single column of vertical velocity from the LES. To avoid fast-moving scalar gradients, numerical stability is maintained through a westward-domain translation that matches the mean-flow velocity of the cloud layer (10 ms^{-1}); correspondingly, the virtual lidars maintain stationarity relative to the domain translation through an eastward translation of 10 ms^{-1} (i.e., one grid box per time-step). The virtual lidars were placed every 100 m in the y-direction (24 lidars), and any individual cloud element could be sampled by more than one lidar. The three-dimensional fields of liquid water content and vertical velocity were output every successive model time-step for 200 s at 30-minute intervals starting at 3.5 hrs (to avoid spin-up contamination). A transect was deemed usable if the empty space at each edge of a cloud chord and the chord length itself was at least 100 m. Each usable virtual lidar transect has a front cloud

edge that corresponds to the specific time when the cloud was first sampled. The three-dimensional file associated with the incidence of the virtual lidar front edge is accessed to ascertain the static cross-section by finding the accompanying back edge and ensuring that the static transects meet the aforementioned chord and empty space criteria.

3 Results and Discussion

3.1 Composite Shell Structure

The most prominent vertical-velocity features observed among all clouds and across both sites consist of a tilted updraft structure and an asymmetric subsiding shell (Figure 1). Given an ascending thermal sampled through time, an upward slope toward the lifted condensation level on the front edge would be expected. However, the mean slope of the updrafts in Figure 1 would imply an average thermal velocity of 5-10 ms^{-1}, suggesting the sloped updraft on the front edge is not solely an artifact of the sampling method. Focusing on the vertical subsiding shell asymmetry, at 200 m in front of the cloud edge the shell structure penetrates ~275 m into the sub-cloud layer, while 200 m behind the back edge the shell penetrates 400 m or more into the sub-cloud layer (Figure 1). Assuming the back-edge shell was initially a mirror image of the front-edge shell - an average subsiding shell intensity of 0.2 ms^{-1} (see supplement Figure S2a), an average horizontal advective velocity of 5 ms^{-1}, and an average chord length of 300 m would result in a back-edge shell that descended 12 m in the time it took the cloud to pass over the lidar. The prior calculation posits that any cloud-evolution effects would be unable to explain the disparity between front and back-edge shell penetration depth, albeit, assuming an average subsiding shell intensity omits the possibility of intermittently intense or accelerating downdrafts. Shell penetration depths on the front and back edges at SGP and JOYCE are

comparable, although the intensities are markedly different with substantially stronger downdrafts at SGP (Figure 1). Except for the differences in vertical velocity intensity, the composite structures of the sites are similar.

The representativeness of the observed composite structure is a function of the underlying vertical velocity distributions. While there is considerable cloud-to-cloud variability, vertical velocity PDFs are not substantially skewed, with distribution means being predominantly influenced by peaks and not elongated tails (see supplement Figure S2). The vertical velocity distributions suggest that the structures observed are expected for a typical shallow cumulus cloud and not a consequence of extreme events.

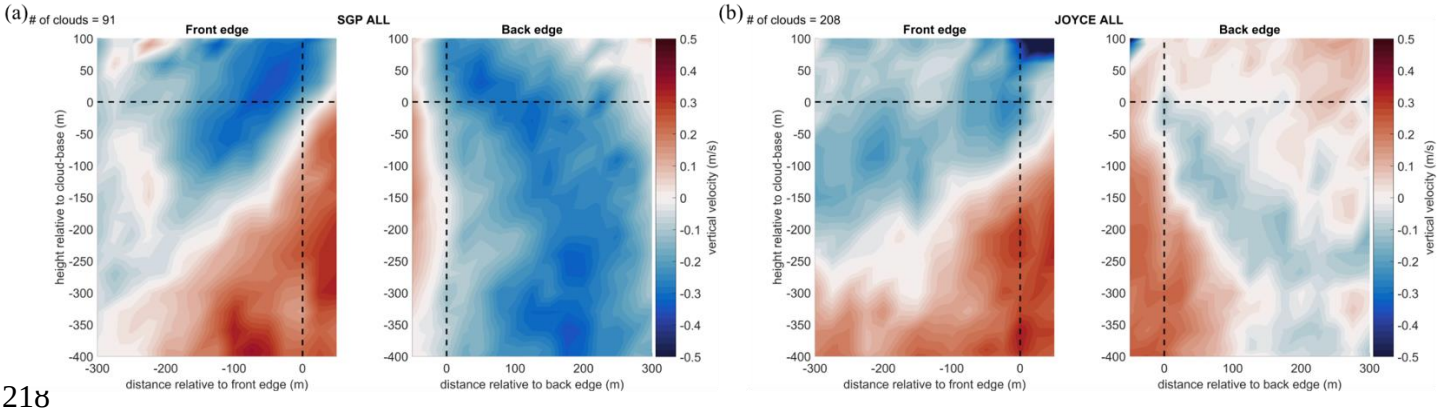

Figure 1: Vertical velocity composites for all clouds observed at (a) SGP and (b) JOYCE. The wind blows from right to left (back edge is upwind). Cloud resides in the first quadrant for the front-edge plots, and in the second quadrant for back-edge plots. Composites are based on 91 clouds sampled at SGP and 208 at JOYCE.

To investigate changes in subsiding shell structure related to cloud stage, cloud chords were separated into positive and negative mass-flux clouds. Positive mass-flux clouds make up approximately 60% and 50% of the total cloud sample at SGP and JOYCE, respectively. The positive mass-flux statistics for SGP are consistent with Lareau et al. (2018) who found positive mass-flux clouds to occur in ~63% of the cloud chords. However, the distribution is not skewed at JOYCE, with each case being equally probable. Positive mass-flux clouds at SGP show a

more pronounced subsiding shell on the front edges in comparison with JOYCE, with a roughly analogous below-cloud subsiding shell structure on the back edges (Figure 2a,c). Updraft structure is homologous in positive mass-flux clouds at SGP and JOYCE, with slightly more vigorous updrafts at SGP (Figure 2a,c). The concept of a subsiding shell with respect to negative mass-flux clouds is obfuscated by the downward motion of the cloud itself, with the subsiding shell possibly being a result of downward drag from the parent cloud's downdraft. Nonetheless, negative mass-flux clouds still manifest regions of enhanced negative vertical velocity near the cloud edges, with a local maximum in shell intensity at the front edge near cloud base found at SGP and JOYCE (Figure 2b,d). The negative mass-flux clouds at SGP show signs of similar asymmetries observed in positive mass-flux clouds, with a broader and deeper shell on the back edge (Figure 2b). However, the typical asymmetry between the front and back edge is not observed at JOYCE, with negative mass-flux clouds possessing a broad and strong subsiding shell on the front edge and a strikingly weaker shell on the back edge (Figure 2d).

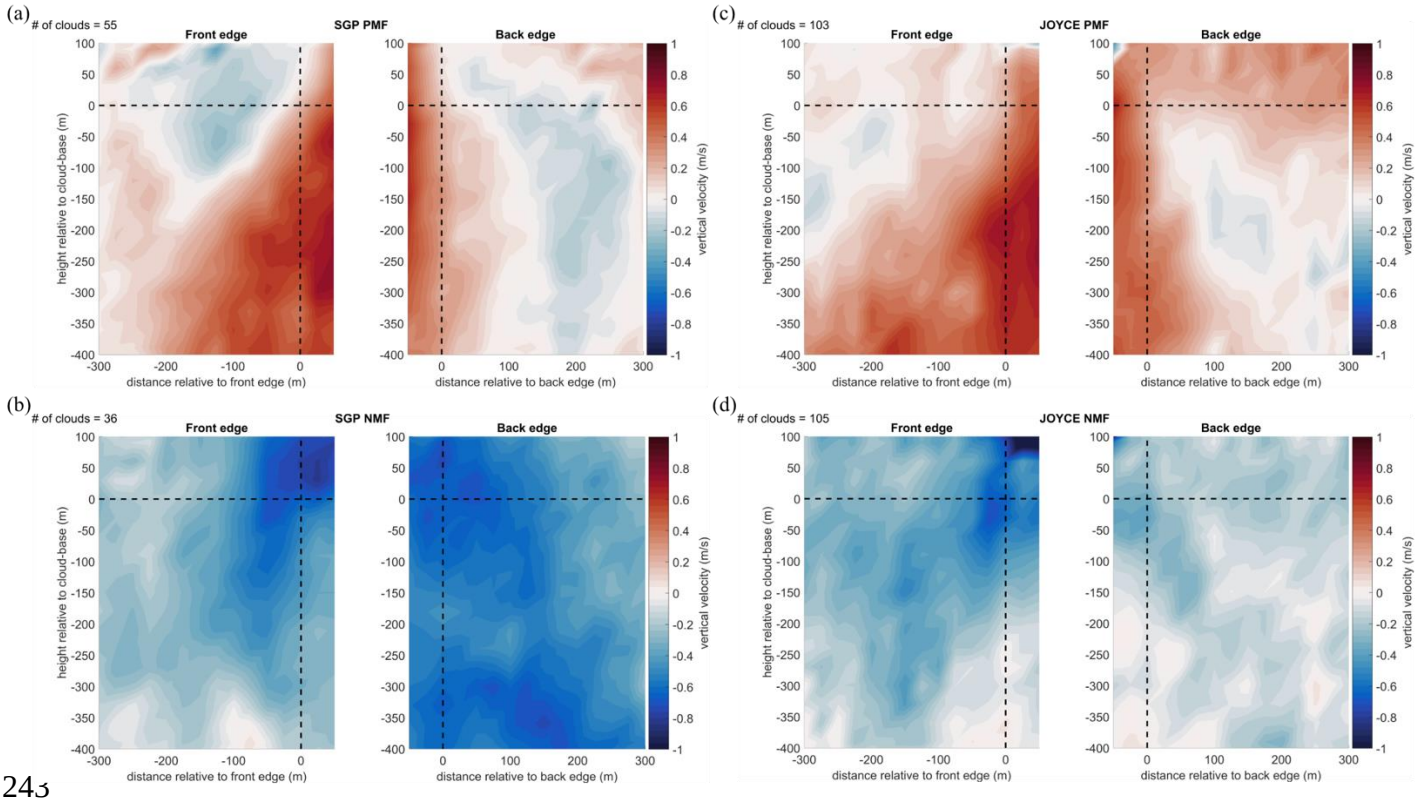

Figure 2: Positive mass-flux (PMF) and negative mass-flux (NMF) clouds at SGP (a, b) and JOYCE (c, d), based on criteria in the text. The wind blows from right to left.

3.1 Average Shell Frequency and Width

Subsiding shells occurred in ~50-70% of all cloud samples at SGP and ~20-40% at JOYCE, with the highest probabilities occurring near cloud base (Figure 3a,c). There are no substantial differences in the probability of shell occurrence between the front and back edges per site, and shell frequency generally increases ~20% from 400 m below cloud base to cloud base (Figure 3a,c). Overall, the frequencies are likely underestimated by obscuration from the highly turbulent flow near the cloud edges and the stringent criteria used to identify the subsiding shells (Section 2.2). The average subsiding shell width for all clouds is ~100 m with little variation with height (Figure 3b,d). There is no discernible difference in average shell width between the front and back edges at SGP, but back edge shells at JOYCE are ~25 m wider than

shells on the front edge (Figure 3b,d). Subsiding shells are wider (~50 m) in negative mass-flux clouds than in positive mass-flux clouds (Figure 3b,d), which agrees with the findings of Katzwinkel et al. (2014).

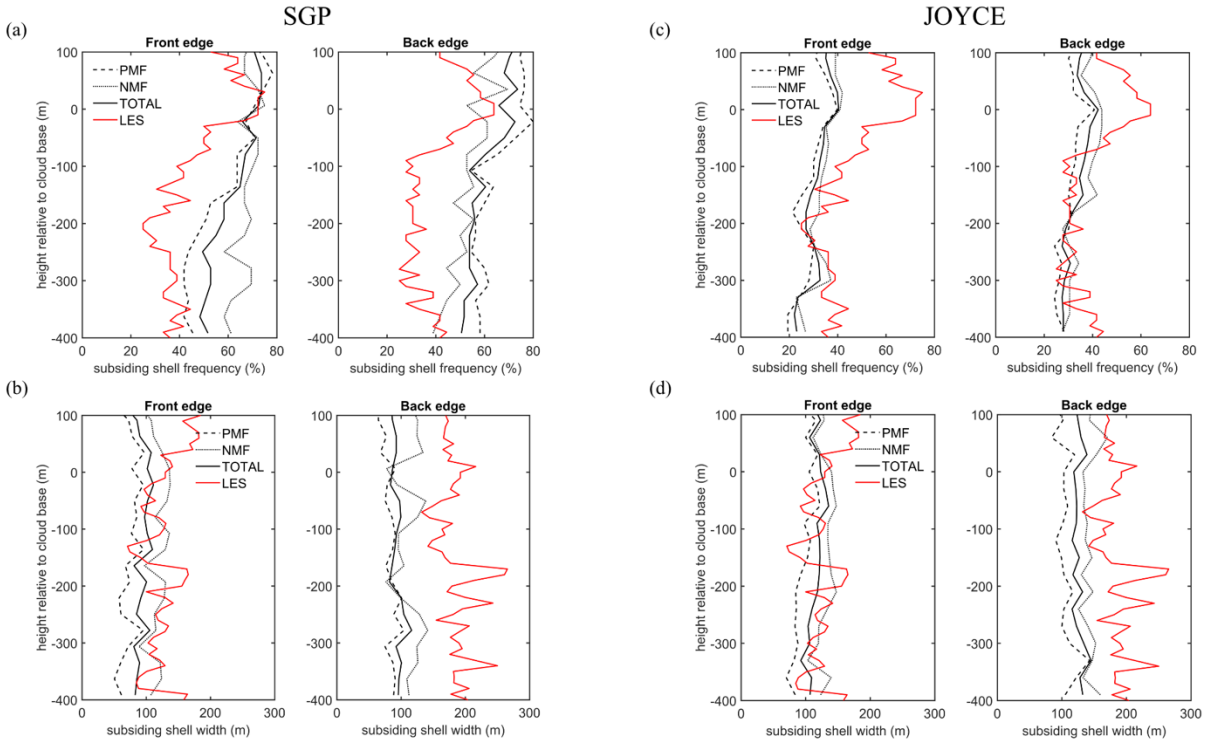

Figure 3: (a, c) Subsiding shell frequency (%) and (b, d) Subsiding shell width (m) for SGP (left) and JOYCE (right). Shown are all clouds at a site (TOTAL; solid black line) and partitioned as positive mass-flux (PMF; dashed) and negative mass-flux (NMF; dotted) clouds. The red line is the LES result.

3.3 Exploration of Asymmetry Using LES

The purpose of the simulations is twofold: (1) determine the fidelity of the LES in generating observed cloud structures and statistics, and (2) examine the effects of transient cloud evolution on observed shell asymmetries. The static cloud transects indicate a stronger subsiding shell on the front edge in comparison to the back edge (Figure 4a). This dynamic asymmetry of shell intensity is in accordance with previous BOMEX simulations and observations of clouds in sheared environments (Heymsfield et al., 1978; Heus and Jonker, 2008), where the updraft core

is displaced toward the back edge (upshear side). The displacement of the updraft induces increased upward drag on the subsiding shell near the back edge, which may explain why the back-edge shell generally has weaker shells (Figure 4a). Additionally, much like a cylinder embedded in a flow, an ascending/descending plume may act as a flow obstacle, and wake turbulence can be generated on the downwind side of the plume (Heymsfield et al., 1978). Another possibility, which remains largely unexplored, is the asymmetry of convective vortex rolls in different flow regimes and the impact this may have on entrainment, momentum, and buoyancy near the cloud edge (Park et al., 2017). Altogether, the back-edge shell is likely weaker because of decreased turbulent mixing (compared to the front edge), increased upward drag from a displaced updraft, and perhaps, a weaker vortex than the front (downshear/downwind) side.

Apart from asymmetry driven by the dynamics, asymmetry may be introduced by cloud evolution when observing clouds passing overhead from a fixed instrument location. The two primary reasons to expect some asymmetry are: (1) the back edge of the cloud is observed at a later time, giving a subsiding shell more time to intensify and penetrate into the sub-cloud layer and (2) direct numerical simulation of actively growing clouds indicate that the shell thickness grows linearly with time (Nair et al., 2019), possibly resulting in a wider than average shell on the back edge.

To address these cloud-evolution effects, we compare the virtual lidar vertical velocity composite to the static vertical velocity composite (Figure 4). The differences in average shell penetration depth between virtual lidar and static transects are negligible, reinforcing the hypothesis that cloud evolution plays a minor role (Figure 4). The virtual lidar transects retain the asymmetry in shell intensity related to the dynamics, with the front-edge shell remaining stronger than the back-edge shell. The front-edge virtual lidar and static composites both exhibit

a sloped updraft structure, resembling the observed structure at SGP and JOYCE (Figure 4). This provides further evidence for the slope of the updraft being a dynamical feature and not a result of cloud evolution. The BOMEX case involves swiftly moving clouds (~10 m/s), and it is reasonable to assume that slower horizontal wind speeds might allow for more appreciable subsiding shell asymmetry given the larger difference in sampling times between front and back edges; however, a classification of observed clouds by horizontal wind speed indicates that stronger horizontal wind speeds maintain the asymmetry (see supplement Figure S3). Additionally, the average chord length of a virtual lidar transect was ~270 m and the average chord length of an observed cloud was ~300 m, suggesting that differences in total sampling times do not explain the lack of cloud-evolution effects in modeled clouds.

The average vertical velocities on the front and back edges for the virtual lidar transects agree well with the vertical velocity composites from SGP and particularly JOYCE; although, the shells on the back edge of the virtual lidar transects do not descend as far into the sub-cloud layer, and the intensities of downdrafts in BOMEX clouds are substantially weaker in comparison to SGP (Figure 4b; Figure 1a). The physical reasoning for the variation of back-edge shell behavior between observed and modeled clouds is currently unknown and requires further work to determine the root cause. It remains possible that stronger vertical velocities observed over land (Endo et al., 2019) lead to more noticeable cloud-evolution effects in comparison to the BOMEX case.

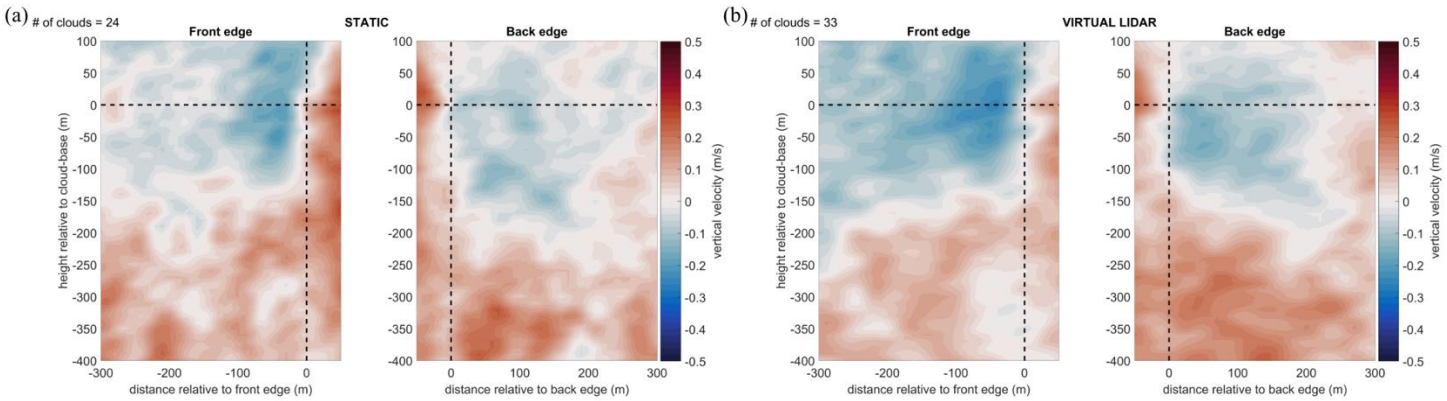

Figure 4: Vertical velocity composites. (a) Static cloud transects (b) Virtual lidar transects. Static results are based on 24 total cloud transects, and virtual lidar results are based on 33 total cloud transects.

LES shell frequency and width statistics were calculated for the static cloud transects (Figure 3; red line). Subsiding shells occur in 30-70% of transects on the front edge and 30-60% on the back edge, with the greatest probability of subsiding shells in close proximity to cloud base, consistent with observed frequencies (Figure 3a; red line). The subsiding shell width is ~100 m on the front edge, with a considerably wider shell width of ~200 m on the back edge. We note that while this comparison is informative, direct comparisons of specific shell characteristics (width, frequency, and penetration depth) between these LES results and observations should be made with caution, as BOMEX is an idealized maritime shallow cumulus environment and the lidar observations represent two unique land surfaces and multiple shallow cumulus environments with varying Bowen ratios and large-scale conditions.

4 Conclusions

This research represents the first attempt to observationally characterize the composite structure of subsiding shells with ground-based Doppler lidar and explore the influence of cloud evolution on shell behavior using high-resolution modeling. Lidar observations of shallow cumulus over the central United States and western Germany demonstrate distinct and recurrent

features resembling an asymmetric subsiding shell, with shells at the back edges of clouds being broader and descending further into the sub-cloud layer compared to those at the front edges. The updrafts are more pronounced on the front edges and tilt upward toward the cloud base. Average vertical velocities in the shells range from -0.1 to -0.4 ms^{-1}, with a similar range for updraft velocities (0.1 to 0.4 ms^{-1}). The frequency of positive mass-flux clouds is found to be ~60% at SGP, reinforcing previous estimates (Lareau et al., 2018), while positive mass-flux clouds at JOYCE occur roughly 50% of the time. Positive mass-flux clouds have stronger front edge subsiding shells at SGP than at JOYCE, with comparable shell intensity on the back edge. Negative mass-flux clouds retain much of the asymmetry seen in positive mass-flux clouds with pronounced subsiding shells on the front edges and broader and deeper shells on the back edge. An exception is for the back-edge shell structure at JOYCE, where the subsiding shell is substantially weaker than the front edge. Subsiding shells occurred in ~20-70% of all cloud samples, with an average width of ~100 m. Negative mass-flux clouds possess shells that are ~50 m wider than positive mass-flux clouds, corroborating the work of Katzwinkel et al. (2014).

Large-eddy simulations of the BOMEX case were performed to address the asymmetries observed in shell structure, and to further examine the ability of the LES to represent subsiding shells. Virtual lidar tests show striking similarities between the LES and Doppler lidar on the front edges, both in terms of shell structure and intensity, but the modeled back-edge shells do not descend as far into the sub-cloud layer as observed clouds. Static cloud transects agree with previous modeling experiments, for which the asymmetries in shell strength were shown to result from shear. The differences between virtual lidar and static transects are minor, thus implying that the observed features are dynamically relevant and not a result of transient cloud evolution.

However, the cloud-evolution effect could be more pronounced in continental clouds with wider vertical velocity PDFs in comparison to the simulated clouds.

We expect the observed shallow cumulus structures to be ubiquitous so long as some shear is present, which is nearly always the case in cumulus boundary layers. The relationship between shear intensity and the degree of asymmetry is not well understood, though, but may be related to the role of updrafts/downdrafts in weakly sheared flows acting as obstacles and the uneven distribution of an upward drag force on the subsiding shell between the front and back edges. Moreover, the dependence of shell strength on convective vortices on the cloud edges and how convective vortices respond to shear warrants further exploration. We speculate that much of the observed asymmetry in shell penetration depth may be a result of convective vortex-ring tilting, a phenomenon that occurs when a vortex ring interacts with a sheared flow (Cheng et al., 2009). Future parameterizations of shallow convection will increasingly rely on the representation of cloud-scale mixing processes, which will require knowledge of the physics of entrainment and the near-cloud environment (subsiding shell region) from which air is entrained.

Acknowledgements and Data

The authors appreciate insightful comments by two anonymous reviewers, which led to additional analysis that greatly improved clarity and justification of our results. Co-authors L.M. and D.M. were funded by U.S. Department of Energy Atmospheric Systems Research Grant DE-SC0016522. JOYCE observations originate from the German Research Foundation (DFG) funded Core Facility JOYCE-CF under DFG Research Grant LO 901/7-1. A.V. was supported by the Climate Model Development and Validation activity funded by the Office of Biological and Environmental Research in the U.S. Department of Energy Office of Science through award KP170304. F.Y. and A.V. were supported by the US Department of Energy (DOE) Atmospheric System Research Program under contract DE-SC0012704. M.T. was supported through the Maj and Tor Nessling Foundation (grant 201700032). Special thanks to the second ARM Training and Science Application Event (https://journals.ametsoc.org/doi/full/10.1175/BAMS-D-18-0242.1), as well as Susanne Crewell for co-leading our research group. SGP lidar data were obtained from the ARM Climate Research Facility, a U.S. Department of Energy Office of Science user facility sponsored by the Office of Biological and Environmental Research. All data

are available from the ARM Data Discovery website (https://www.archive.arm.gov/discovery/). JOYCE lidar data can be obtained online (http://cpex-lab.de/cpex-lab/EN/Home/JOYCE-CF/JOYCE-CF_node.html). LES model configuration files (DOI: 10.5281/zenodo.3774571) and LES cloud transect data (DOI:10.5281/zenodo.3779540) can be found at the provided links.

References

Ansmann, A., Fruntke, J. and Engelmann, R. (2010). Updraft and downdraft characterization with Doppler lidar: Cloud-free versus cumuli-topped mixed layer, *Atmos. Chem. Phys.*, **10**(16), 7845–7858.

Arakawa, A. and Schubert, W. H. (1974). Interaction of a Cumulus Cloud Ensemble with the Large-Scale Environment, Part I. *J. Atmos. Sci.*, **31**, 674–701.

Bony, S., et al. (2015). Clouds, circulation and climate sensitivity, *Nat. Geosci.*, **8**, 261–268.

Bretherton, C. S., Blossey, P. N. and Jones, C. R. (2013). Mechanisms of marine low cloud sensitivity to idealized climate perturbations: A single LES exploration extending the CGILS cases. *J. Adv. Model. Earth Syst.*, **5**, 316–337, doi:10.1002/jame.20019.

Caldwell, P. M., Zelinka, M. D., Taylor, K. E. and Marvel, K. (2016). Quantifying the Sources of Intermodel Spread in Equilibrium Climate Sensitivity. *J. Climate*, **29**, 513–524.

Ceppi, P., Brient, F., Zelinka, M. D. and Hartmann, D. L. (2017). Cloud feedback mechanisms and their representation in global climate models. *WIREs Clim Change*, 8: e465. doi:10.1002/wcc.465

Chen, T., Rossow, W. B. and Zhang, Y. C. (2000). Radiative effects of cloudtype variations. *J. Climate*, **13**, 264–286, doi:10.1175/1520-0442 (2000)013<0264:RE OCTV>2.0.CO;2.

Cheng, M., Lou, J. and Lim, T. T. (2009). Motion of a vortex ring in a simple shear flow. *Physics of Fluids*, **21**, https://doi.org/10.1063/1.3196903

Clothiaux, E. E., Ackerman, T. P., Mace, G. G., Moran, K. P., Marchand, R. T., Miller, M. A., and Martner, B. E. (2000). Objective determination of cloud heights and radar reflectivities using a combination of active remote sensors at the ARM CART sites, *J. Appl. Meteorol*., 39, 645.

de Rooy, W. C., Bechtold, P., Fröhlich, K., Hohenegger, C., Jonker, H., Mironov, D., Siebesma, A. P., Teixeira, J. and Yano, J.-I. (2013). Entrainment and detrainment in cumulus convection: An overview, *Q. J. R. Meteorol. Soc.*, **139**(670), 1–19.

Deardoff, J. (1980). Stratocumulus-capped mixed layers derived from a three-dimensional model. Boundary-Layer Meteorology, 18, 495–527.

Dufresne, J. and Bony, S. (2008). An Assessment of the Primary Sources of Spread of Global Warming Estimates from Coupled Atmosphere–Ocean Models. *J. Climate*, **21**, 5135–5144.

Endo, S., Zhang, D., Vogelmann, A. M., Kollias, P., Lamer, K., Oue, M., et al. (2019). Reconciling differences between large-eddy simulations and Doppler lidar observations of continental shallow cumulus cloud-base vertical velocity. *Geophysical Research Letters*, **46**, https://doi.org/10.1029/2019GL084893

Heus, T. and Jonker, H. J. (2008). Subsiding Shells around Shallow Cumulus Clouds. *J. Atmos. Sci.*, **65**, 1003–1018, https://doi.org/10.1175/2007JAS2322.1

Heymsfield, A. J., Johnson, P. N., and Dye, J. E. (1978). Observations of Moist Adiabatic Ascent in Northeast Colorado Cumulus Congestus Clouds. *J. Atmos. Sci.*, **35**, 1689–1703, https://doi.org/10.1175/1520-0469(1978)035<1689:OOMAAI>2.0.CO;2

Hogan, R. J., Behera, M. D., O'Connor, E. J., & Illingworth, A. J. (2004). Estimate of the global distribution of stratiform supercooled liquid water clouds using the LITE lidar. *Geophys. Res. Lett.*, **31**, L05106. https://doi.org/10.1029/2003GL018977

Holland, J. Z. and Rasmusson, E. M. (1973). Measurements of the Atmospheric Mass, Energy, and Momentum Budgets Over a 500-Kilometer Square of Tropical Ocean. Mon. Wea. Rev., 101, 44–55.

Illingworth, A. J., Hogan, R. J., O'Connor, E., Bouniol, D., Brooks, M. E., Delanoé, J., Donovan, D. P, Eastment, J. D., Gaussiat, N., Goddard, J. W., Haeffelin, M., Baltink, H. K., Krasnov, O. A., Pelon, J., Piriou, J., Protat, A., Russchenberg, H. W., Seifert, A., Tompkins, A. M., van Zadelhoff, G., Vinit, F., Willén, U., Wilson, D. R., and Wrench, C. R. (2007). Cloudnet. *Bull. Amer. Meteor. Soc.*, **88**, 883–898, https://doi.org/10.1175/BAMS-88-6-883

Jonas, P. R. (1990). Observations of cumulus cloud entrainment. *Atmospheric Research*, **25**, 105-127, https://doi.org/10.1016/0169-8095(90)90008-Z

Jonker, H. J., Heus, T. and Sullivan, P. P. (2008). A refined view of vertical mass transport by cumulus convection, *Geophys. Res. Lett*., **35**, L07810, doi:10.1029/2007GL032606.

Katzwinkel, J., Siebert, H., Heus, T., and Shaw, R. A. (2014). Measurements of Turbulent Mixing and Subsiding Shells in Trade Wind Cumuli. *J. Atmos. Sci.*, **71**, 2810–2822, https://doi.org/10.1175/JAS-D-13-0222.1.

Khairoutdinov, M. F. and Randall, D. A. (2003). Cloud resolving modeling of the ARM summer 1997 IOP: model formulation, results, uncertainties, and sensitivities. Journal of the Atmospheric Sciences, 60, 607–625.

Klinger, C., Mayer, B., Jakub, F., Zinner, T., Park, S.-B. and Gentine, P. (2017). Effects of 3-D thermal radiation on the development of a shallow cumulus cloud field. *Atmos. Chem. and Phys.*, **17**, 5477-5500.

Kollias, P., B. A. Albrecht, E. E. Clothiaux, M. A. Miller, K. L. Johnson, and K. P. Moran (2005). The atmospheric radiation measurement program cloud profiling radars: An evaluation of signal processing and sampling strategies, *J. Atmos. Oceanic Technol*., 22, 930–948.

Lamer, K. and Kollias, P. (2015). Observations of fair-weather cumuli over land: Dynamical factors controlling cloud size and cover, *Geophys. Res. Lett.*, **42**, 8693–8701, doi:10.1002/2015GL064534

Lareau, N. P., Zhang, Y. and Klein, S. A. (2018). Observed Boundary Layer Controls on Shallow Cumulus at the ARM Southern Great Plains Site. *J. Atmos. Sci.,* **75**, 2235–2255, https://doi.org/10.1175/JAS-D-17-0244.1

Löhnert, U., Schween, J. H., Acquistapace, C., Ebell, K., Maahn, M., Barrera-Verdejo, M., Hirsikko, A., Bohn, B., Knaps, A., O'Connor, E., Simmer, C., Wahner, A. and Crewell, S. (2015). JOYCE: Jülich Observatory for Cloud Evolution. *Bull. Amer. Meteor. Soc.*, **96**, 1157–1174, https://doi.org/10.1175/BAMS-D-14-00105.1

Maslin, M. and Austin, P. (2012). Climate Models at Their Limit? *Nature*, **483**, 183-184.

Nair, V., Heus, T. and van Reeuwijk, M. (2019). Dynamics of Subsiding Shells In Actively Growing Clouds With Vertical Updrafts. *J. Atmos. Sci.,* **0**, https://doi.org/10.1175/JAS-D-19-0018.1

Newsom, R. K. (2012). Doppler lidar handbook. Technical Report, DOE/SC-ARM-TR-101, DOE ARM Research Facility, 16 pp. https://doi. org/10.2172/1034640

Park, S.-B., Heus, T. and Gentine, P. (2017). Role of convective mixing and evaporative cooling in shallow convection, *J. Geophys. Res. Atmos*., **122**, 5351–5363, doi:10.1002/2017JD026466.

Rodts, S. M., Duynkerke, P. G. and Jonker, H. J. (2003). Size Distributions and Dynamical Properties of Shallow Cumulus Clouds from Aircraft Observations and Satellite Data. *J. Atmos. Sci.,* **60**, 1895–1912.

Rossow, W. B. and Schiffer, R. A. (1999). Advances in Understanding Clouds from ISCCP. *Bull. Amer. Meteor. Soc.,* **80**, 2261–2288.

Satoh, M., Stevens, B., Judt, F., Khairoutdinov, M., Lin, S.-J., Putnam, W. M. and Duben, P. (2019). Global Cloud-Resolving Models. *Curr. Clim. Change. Rep.*, 5, 172, https://doi.org/10.1007/s40641-019-00131-0

Sherwood, S. C., Bony, S. and Dufresne, J.-L. (2014). Spread in model climate sensitivity traced to atmospheric convective mixing. **Nature**, *505*, 37-42.

Stevens, B. and Bony, S. (2013). What are Climate Models Missing? *Science*, **340**, 1053-1054.

Wyant, M. C., Bretherton, C. S. and Blossey, P. N. (2009). Subtropical Low Cloud Response to a Warmer Climate in a Superparameterized Climate Model. Part I: Regime Sorting and Physical Mechanisms. *J. Adv. Model. Earth Syst*., **7**, doi:10.3894/JAMES.2009.1.7.

Yamaguchi, T., Randall, D. A. and Khairoutdinov, M. F. (2011). Cloud modeling tests of the ultimate-macho scalar advection scheme. MonthlyWeather Review, 139, 3248–3264.

Yano, J.-I., et al. (2015). Basic concepts for convection parameterization in weather forecast and climate models: COST action ES0905 final report. *Atmosphere*, **6**, 88–147.

Zelinka, M. D., Zhou, C. and Klein, S. A. (2016). Insights from a refined decomposition of cloud feedbacks. *Geophys. Res. Lett.*, **43**, 9259–9269, doi:10.1002/2016GL069917.

Zelinka, M. D., Myers, T. A., McCoy, D. T., Po-Chedley, S., Caldwell, P. M., Ceppi, P., et al. (2020). Causes of higher climate sensitivity in CMIP6 models. *Geophysical Research Letters*, **47**, e2019GL085782. https://doi.org/10.1029/2019GL085782

Supporting Information for:

Characterizing subsiding shells in shallow cumulus using Doppler lidar and large-eddy simulation

Lucas A. McMichael[1], Fan Yang[2], Tobias Marke[3,4], Ulrich Löhnert[5], David B. Mechem[1], Andrew M. Vogelmann[2], Kevin Sanchez[6,7], Minttu Tuononen[8,9], and Jan H. Schween[5]

1 Department of Geography and Atmospheric Science, University of Kansas, Lawrence, KS, USA
2 Environmental and Climate Sciences Department, Brookhaven National Laboratory, Upton, NY, USA
3 Cooperative Institute for Research in Environmental Sciences, University of Colorado, Boulder, CO, USA
4 NOAA/Earth System Research Laboratory, Chemical Sciences Laboratory, Boulder, CO, USA
5 Institute for Geophysics and Meteorology, University of Cologne, Cologne, Germany
6 Universities Space Research Association, Columbia, MD, USA
7 NASA Langley Research Center, Hampton, VA, USA
8 Finnish Meteorological Institute, Helsinki, Finland
9 Vaisala Oyj, Vantaa, Finland

Contents of this file

Text S1 and S2
Figures S1, S2, and S3

Additional Supporting Information (Files uploaded separately)

N/A

Introduction

The supporting information includes a discussion of observational limitations with lidars (Text S1), specifics of LES BOMEX configuration (Text S2), cloud-base vertical velocity PDFs for 10 and 25 m grid spacing (Figure S1), vertical velocity PDFs for front and back edges (Figure S2), and classification of observed clouds by horizontal wind speed at SGP and JOYCE (Figure S3).

Text S1: Observational Limitations

The method used to map from time to space is estimated by assuming the mean velocity field dominates the contribution of the horizontal advection from the individual eddies (Taylor's hypothesis). The use of Taylor's hypothesis should capture the general structure of subsiding shells without having to account for the complex horizontal velocity structure within the turbulent boundary layer. There was no automated constraint on the cloud-top height, so deeper clouds (>1 km in depth) may have been included in the analysis. Additionally, the lidar randomly samples the cloud field, which means the probability of a transect being directly through the cloud center is unlikely, making the unambiguous distinction between negative and positive mass-flux clouds difficult.

Text S2: Model Configuration

The prognostic equations for momentum are stepped forward in time using the third-order Adams-Bashforth time-differencing method. Scalar advection is performed with a fifth-order advection scheme (ULTIMATE-MACHO; Yamaguchi et al., 2011). The subgrid-scale turbulent fluxes are based on the prognostic, 1.5-order TKE closure developed by Deardoff (1980). Vertical damping of waves is performed on the top 30% of the domain with a Rayleigh sponge layer. To maintain consistency between the observed and modeled clouds, precipitation is not permitted and the condensation scheme assumes a simple saturation adjustment. Surface fluxes are held constant for the duration of the run (6 h) and the Coriolis force is neglected. Radiative cooling and large-scale subsidence is prescribed.

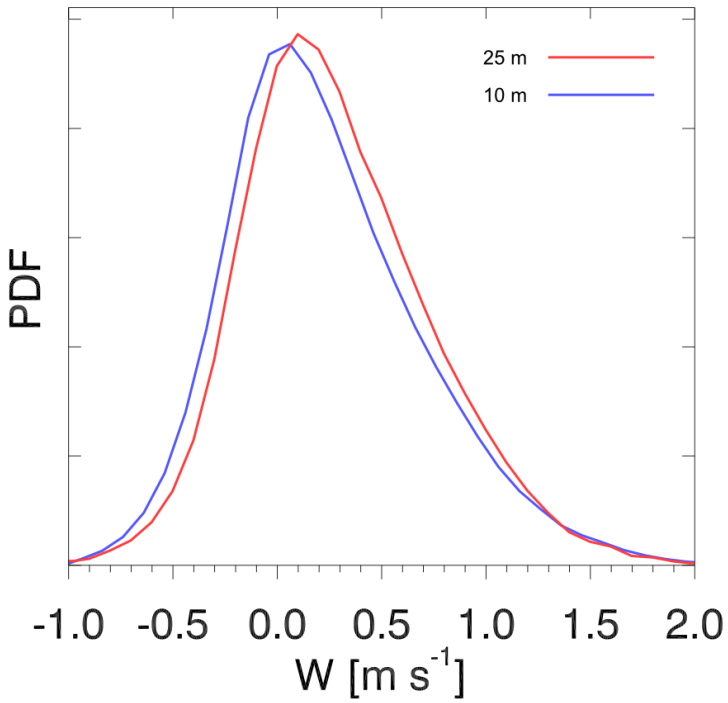

Figure S1: Cloud-base vertical velocity PDF for 10 m grid spacing (blue) and 25 m grid spacing (red).

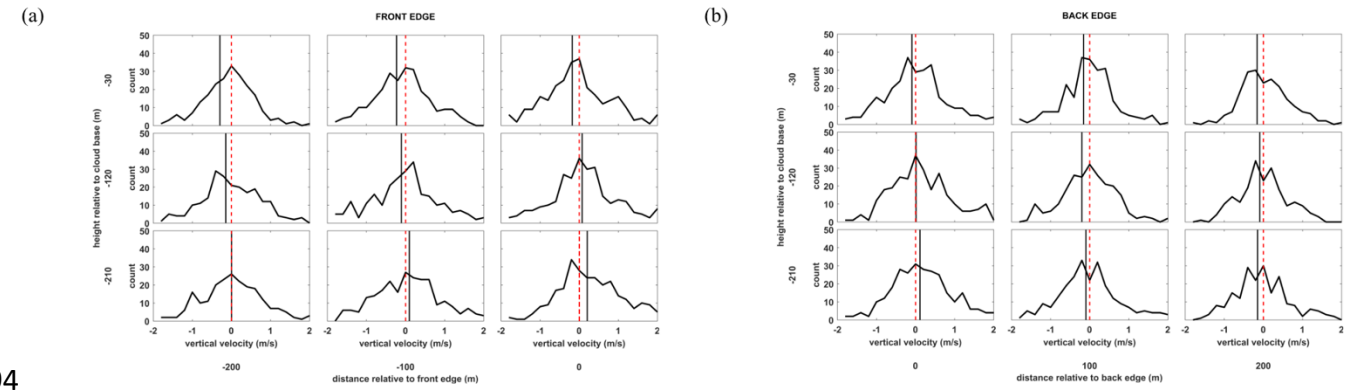

Figure S2: Vertical velocity PDFs (SGP and JOYCE clouds combined) in the sub-cloud region (a) front edge and (b) back edge. Vertical black line indicates the PDF mean, while the vertical dashed red line is the zero.

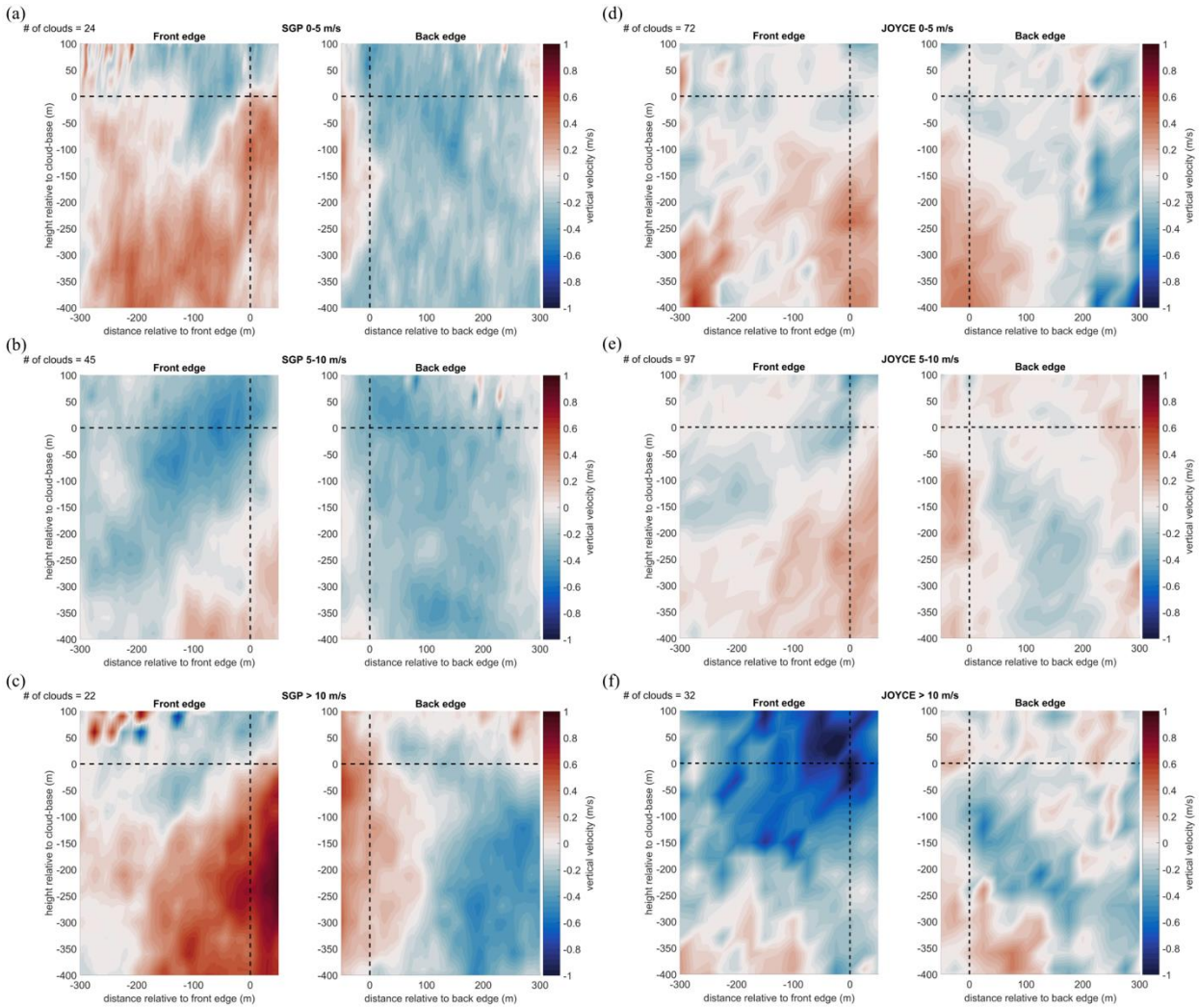

Figure S3: Left column: SGP vertical velocity composites classified by cloud-base horizontal wind speed: (a) low wind speed (0-5 m/s), (b) medium wind speed (5-10 m/s), and (c) high wind speed (>10 m/s). Right column: JOYCE vertical velocity composites classified by cloud-base horizontal wind speed: (d) low wind speed (0-5 m/s), (e) medium wind speed (5-10 m/s), and (f) high wind speed (>10 m/s).